Nanoscale Res Lett (2009) 4:1286–1296
DOI 10.1007/s11671-009-9394-7

NANO EXPRESS

Mesomorphic Lamella Rolling of Au in Vacuum

Chang-Ning Huang · Shuei-Yuan Chen · Pouyan Shen

Received: 22 June 2009 / Accepted: 7 July 2009 / Published online: 18 July 2009

Abstract Lamellar nanocondensates in partial epitaxy with larger-sized multiply twinned particles (MTPs) or alternatively in the form of multiple-walled tubes (MWTs) having nothing to do with MTP were produced by the very energetic pulse laser ablation of Au target in vacuum under specified power density and pulses. Transmission electron microscopic observations revealed (111)-motif diffraction and low-angle scattering. They correspond to layer interspacing (0.241–0.192 nm) and the nearest neighbor distance (ca. 0.74–0.55 nm) of atom clusters within the layer, respectively, for the lamella, which shows interspacing contraction with decreasing particle size under the influence of surface stress and rolls up upon electron irradiation. The uncapped MWT has nearly concentric amorphous layers interspaced by 0.458–0.335 nm depending on dislocation distribution and becomes spherical onions for surface-area reduction upon electron dosage. Analogous to graphene-derived tubular materials, the lamella-derived MWT of Au could have pentagon–hexagon pair at its zigzag junction and useful optoelectronic properties worthy of exploration.

Keywords Gold · Nanocondensates · Lamella · Multiple-walled tubes · Vacuum

C.-N. Huang · P. Shen (✉)
Institute of Materials Science and Engineering, Department of Materials and Optoelectronic Science, Center for Nanoscience and Nanotechnology, National Sun Yat-sen University, Kaohsiung, Taiwan, ROC
e-mail: pshen@mail.nsysu.edu.tw

S.-Y. Chen
Department of Mechanical and Automation Engineering, I-Shou University, Kaohsiung, Taiwan, ROC

Introduction

The motivation of this research is to prove by experiments that a dynamic pulsed laser ablation (PLA) (c) process without the presence of stabilizer or liquid such as in vacuum environment is able to produce intrinsic lamellar Au, which rolled automatically into tubular materials.

Pure ambient Au forms, in the order of decreasing particle size, a face-centered cubic (fcc) structure, an anomalous multiply twinned particle (MTP) of decahedral (Dh) and icosahedron (Ih) types [1, 2], and structural motifs of atom cluster with planar, cage, or pyramid structures [3–5]. In general, such Au nanoparticles melt at a rather low temperature (down to ca. 700 K) [6] to form the entropy-favored 3-D liquid Au clusters. On the other hand, quantum molecular dynamic simulation results [7] suggested that such 3-D clusters would tend to supercool and solidify into 2-D, i.e., freestanding planar liquid phase under an experimentally realizable cooling rate. Such a novel situation of liquid–liquid coexistence and related supercooling, however, awaits experimental proof.

PLA with a very rapid heating/cooling and hence pressure effect was used to synthesize dense dioxide nanocondensates with considerable internal stress [8]. Following this dynamic PLA route, the effect of laser power density and carbon catalysis on the MTP→fcc transformation and phase behavior of the Au nanocondensates was characterized [9]. The nanocondensates were found to contain atom clusters besides larger-sized MTP and fcc when fabricated at a relatively high-power density [9]. The Au atom clusters, MTPs, and fcc nanoparticles when fabricated alternatively by PLA in water were found to develop into mesomorphic lamella and multiple-walled tubes (MWTs) upon aging at room temperature in water [10]. However, it is not clear whether the formation of the lamellar and MWT Au has

anything to do with water molecules. Here, we used PLA in vacuum to clarify that the formation of mesomorphic Au lamellar phase can be intrinsic without the assistance of a liquid phase. We focused on its rolling into MWT under specified laser pulses and power density. The varied lamella interspacing as a function of domain size and the crystallographic relationship between the rolled lamella and MTP formed by condensation and electron irradiation were also addressed.

Experimental Section

Synthesis of Gold Nanocondensate

To produce Au condensates, Au (99.99% pure, 0.3 mm in thickness) foil was subjected to energetic Nd-YAG-laser (Lotis, 1,064 nm in wavelength, beam mode: TEM00) pulse irradiation inside an ablation chamber in vacuum (3.5×10^{-5} torr). The laser ablation parameters that significantly affected phase assemblages and particle size of the condensed Au nanoparticles were compiled in Table 1 of Ref. [9]. It should be noted that the condition used to fabricate atom clusters besides MTP and fcc nanocondensates ca. 5.0 nm in diameter on average at a relatively high-power density of 1.4×10^{12} W/cm^2 (i.e., pulsed energy 650 mJ/pulse; pulse duration 16 ns; beam size 0.03 mm^2; fluence 2.2 kJ/cm^2; frequency 10 Hz under Q-switch mode) [9] was adopted but with lower pulses down to 100 (Table 1) in order to further explore the varied extent of rolling of the lamellae derived from such atom clusters. The atom clusters and lamellae would otherwise be obscured when higher pulses were adopted as the case shown in Fig. 6a of our earlier paper [9].

Characterization

Copper grids overlaid with a carbon-coated collodion film and fixed in position by a plastic holder at a distance of 25–100 mm from the target were used to collect the Au condensates. The composition and crystal structures of the condensates were characterized by field-emission transmission electron microscopy (TEM, FEI Tecnai G2 F20 at 200 kV) with selected-area electron diffraction (SAED) and point-count energy dispersive X-ray (EDX) analysis at a beam size of 1 nm. A large (680 mm) camera length coupled with intensity line profile subtraction of possible artifacts from a blank sample, i.e., a carbon-coated collodion film, and Gauss fitting commonly accepted for the analysis of an electron diffraction intensity profile were employed to resolve low-angle scattering intensity and an additional diffraction of the lamellar phase, the latter being nearly superimposed with {111} of the predominant MTP and minor fcc structure. The electron-beam current density was reduced to about 35 A cm^{-2} for the present TEM observations. Under such electron irradiation conditions in vacuum, the lamellar Au survived and underwent Brownian-type motion [9] analogous to thermally activated migration of fcc Au crystallites on KCl (100) substrate [11, 12]. The sample holder temperature was not controlled during the electron radiation. However, under similar TEM-operating condition (200 kV and a beam current density near 35 A cm^{-2}), the actual sample temperature was measured to be approximately 50 °C by the thermocouple readout [13]. It is, therefore, reasonable to believe that the electron-beam heating effect was about the same extent to activate the movement of mesomorphic gold nanoparticles [9] and lamellae. In any case, the knock-on displacement events for sample thinning as commonly encountered under high-energy MeV electron irradiation [14, 15] does not apply to the present TEM observations at 200 kV.

A UV–vis spectrophotometer (U-3900H, Hitachi) operating at an instrumental resolution of 0.1 nm in the range of 300–800 nm was used to characterize ambient absorption spectra of the condensates overlaid on a silica glass substrate. It should be noted that the lamella Au was deposited separately on carbon-coated collodion film and glass substrate for TEM and spectroscopic observations, respectively. Different bonding surfaces of glass and carbon-coated collodion film are expected to cause change in the lamellar Au near the substrate as demonstrated by carbon catalysis on the MTP-fcc transformation of Au during TEM observations [9]. This substrate effect was, however, negligible for the most lamellar Au deposited to a considerable thickness to be away from the substrate.

The condensates turned out to be finer in size and richer in metastable MTP and even nonstable phases when fabricated under lower laser pulses at a specified power density of 1.4×10^{12} W/cm^2 (Table 1). The nonstable phases include Au clusters and a new mesomorphic lamellar structure with varied extent of rolling, according to the following TEM observations.

Table 1 Pulse-dependent phase and mean particle size (nm) of Au at a specified power density of 1.4×10^{12} W/cm^2

Pulse	100	300	600	900
Phase	C/L > MTP	C/L ~ MTP	C/L < MTP/f	L < MTP/f
Size	2.3	3.4	3.8	4.3

L lamellae with varied extent of rolling, *MTP* multiply twinned particle, *C* cluster of atoms, *f* face-centered cubic

Results

Figure 1a shows the TEM bright field image (BFI) of the distinct MTP/fcc and supercooled Au atom clusters with poor diffraction contrast as produced by laser ablation at 300 or fewer pulses. The atom clusters caused a low-angle electron diffraction halo (Fig. 1a, inset), analogous to that of the polished Beilby layers [16] or Au foil on the verge of melting [17]. Such clusters can hardly be imaged using the low-angle scattering halo (Fig. 1b) or extra diffractions nearly superimposed with the strong {111}-motif and {200} diffractions of the MTP (Fig. 1c) because of local interferences of scattered beams by the amorphous supporting film. The assembly of atom clusters as mesomorphic lamellar structure was, however, manifested by the analysis of lattice images shown later. The diffraction intensity profile and Gauss fits (Fig. 1d) showed that the low-angle scattering falls in the range of 1.36–1.83 Q^{-1} full width at half-height (FWHH). (According to the diffraction intensity profile (added as Appendix 1), there is indeed a low-angle scattering diffraction (a local small bump) in the range of 1.36–1.83 Q^{-1} full width at half-height (FWHH) after background subtraction. This low-angle scattering can be reasonably attributed to Au atom clusters analogous to that of the polished Beilby layers [16] or Au foil on the verge of melting [17] as mentioned.) The extra diffraction of the mesomorphic phase is expected to appear as a shoulder ranging from 4.03 to 4.34 Q^{-1} FWHH at lower diffraction

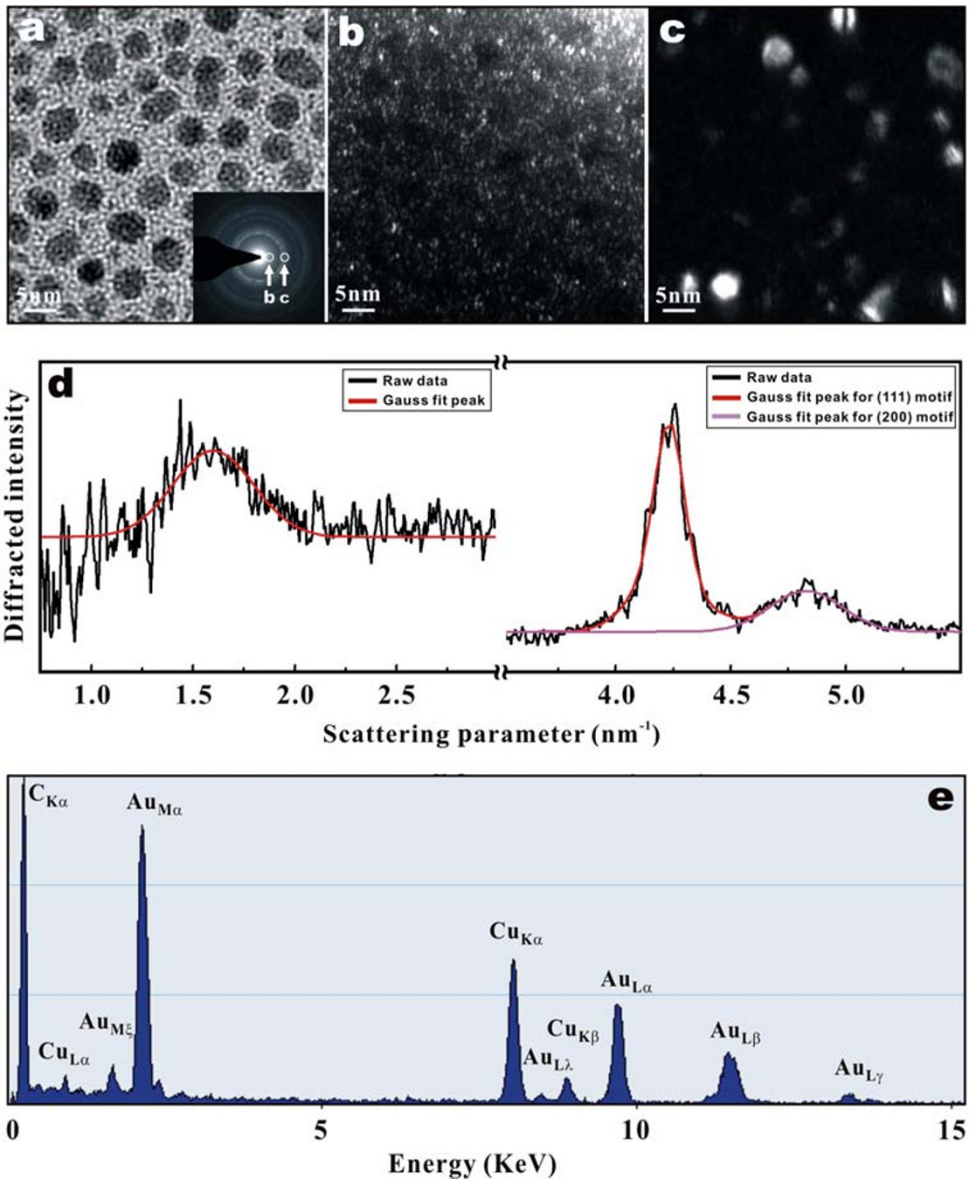

Fig. 1 TEM of Au nanocondensates produced by laser ablation on Au target at 1.4×10^{12} W/cm^2 for 300 pulses in vacuum: **a** BFI, **b** and **c** *dark field images* using low-angle scattering and nearly superimposed {111}/{200} diffractions, respectively, as *circled* in SAED pattern inset in (**a**) with corresponding intensity profiles and Gauss fit to show low-angle scattering of the lamellar phase and (111)/(200) peaks of Au atom clusters and MTP/fcc nanoparticles superimposed with the lamellar basal diffraction in (**d**). **e** Point-count EDX spectrum of the area free of MTP showing Au counts with negligible O and impurities. The Cu count is from the sample supporting copper grid and C from carbon-coated collodion film

angle of the {111}-motif, the other shoulder at higher diffraction angle being characteristic of MTP in view of simulations [18] and experimental studies on size-selected Au nanoparticles [19]. However, a rotational averaging of the integration along the diffraction rings to improve the signal/noise ratio is difficult, if not impossible, due to the superimposed diffraction spots of MTP/fcc, to prove this. Therefore, overinterpretation of the diffraction peak "shoulder" in diffraction line profile should be avoided. EDX analysis on the mesomorphic phase (Fig. 1e) showed Au peaks, with the remaining peaks from the supporting carbon-coated collodion film and Cu grid, indicating that MTP Au is also contributing to the EDS signal by a beam-broadening effect [20]. This result indicates that oxidation or contamination of the Au nanocondensates is negligible.

The extra diffraction almost hidden by {111}-motif showed only for the sample produced under a high-power density of 1.4×10^{12} W/cm^2 [9], and it can be reasonably attributed to 1-D periodicity of the new lamellar phase as indicated by lattice image coupled with 2-D Fourier transform from areas arrowed in Fig. 2a. In such areas, the lamellar domains were developed into the following microstructures, possibly in a sequential manner: mixing with atom clusters (Fig. 2b); coarsening considerably without forming dislocations (Fig. 2c); attaching almost perfectly on the basal layer yet imperfectly at edges (Fig. 2d); and following partial epitaxial relationship with MTP, i.e., having the modulated layers of the lamella parallel to the {111} of MTP, in fact Dh in this case (Fig. 2e). The observed lattice fringes edge-on indicated that the wavelength λ of the mesomorphic lamellae varies from 0.241 to 0.192 nm as the particle size decreases (Fig. 2a, inset), corresponding to 4.03–4.34 Q^{-1} FWHH in the intensity profile (Fig. 1d). By contrast, the (111) motif of MTP has less varied interspacing, ca. 0.234 ± 0.001 nm, according to FWHH of the intensity profile. (Fluctuations in the apparent spacing of Au lamella in local areas b, c, d, and e in Fig. 2a are too wide to fit the (111)- and (200)-motif of MTP/fcc particles. Besides, the fluctuations were measured from local areas away from such particles.) The Au lamella has a fair rigidity yet flexible to roll up. For example, upon electron irradiation for 15 min, the lamellae rolled up as an onion-like shell around the MTP (Fig. 3a). The magnified image coupled with 2-D Fourier transform clearly shows that the curved multiple layers of the lamellae surround the MTP for a partial epitaxial relationship (Fig. 3b). In general, the lamella interspacing was relaxed to slightly higher values (0.238–0.209 nm) (Fig. 3c) and became corrugated near the denser MTP (Fig. 3d). (Depending on the imaging conditions, in particular the diffraction conditions (crystal orientation) and objective lens defocus when the illumination coherence is high enough with a field emission gun, strong symmetrical (111) and ($\overline{111}$) reflections may show up on the opposite sides of the MTP/fcc particle as in the defocused local area of Fig. 3a. However, the areas b, c, and d in Fig. 3a showed

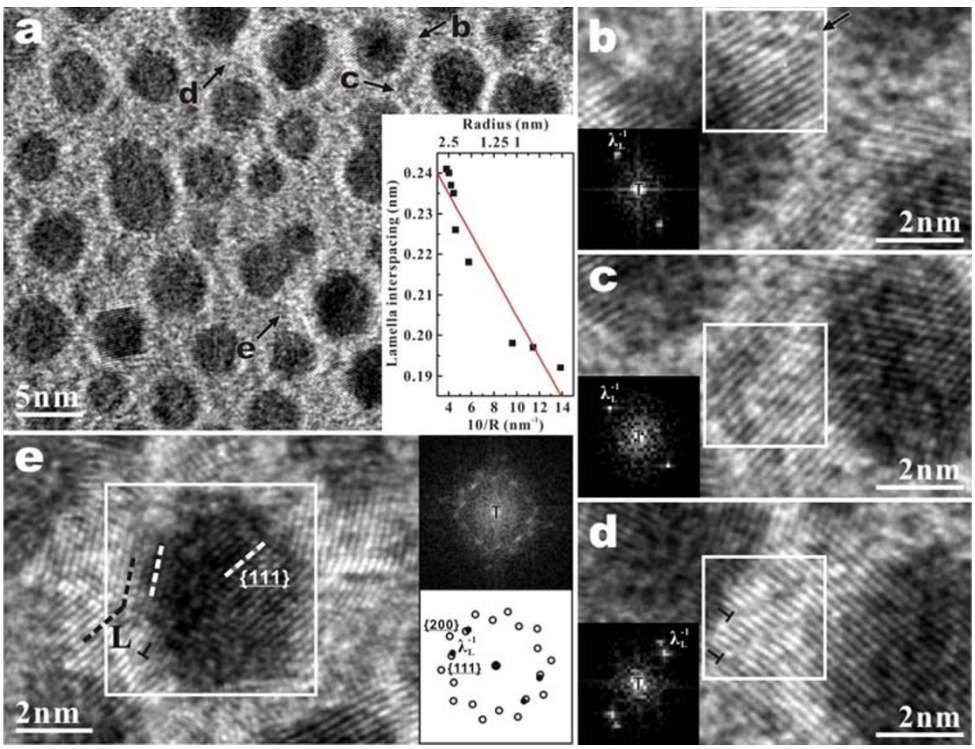

Fig. 2 **a** Lattice image of the as-condensed MTP and lamella (denoted as *L*) with varied interspacing as a function of the reciprocal domain radius, R inset. The lamella in the magnified areas (**b**) to (**e**) coupled with 2-D Fourier transform of the *square region* inset shows that it is associated with atom clusters (*arrow*) in (**b**), considerably coarsened with negligible dislocations in (**c**), imperfectly impinged to form dislocations (denoted by *T*) in (**d**), and in partial epitaxy with MTP, Dh in this case, as indicated by schematic indexing of the reciprocal lamellar interspacing λ_L^{-1} and the diffractions of MTP in (**e**). The same specimen as Fig. 1

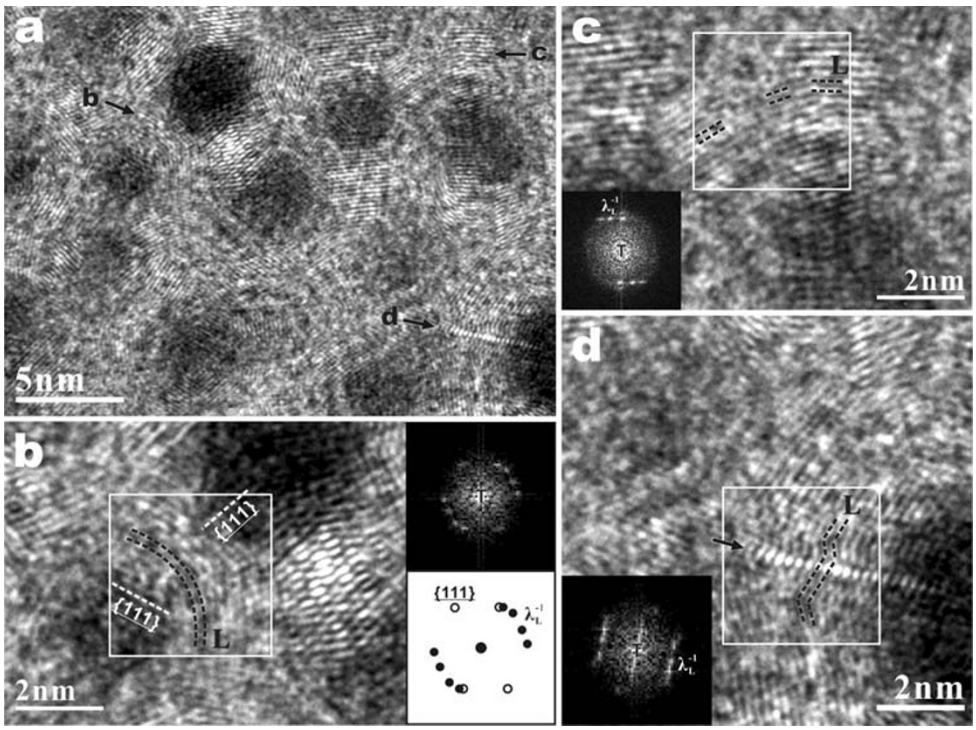

Fig. 3 **a** Lattice image of the lamella and partial epitaxial MTP of the same sample as in Fig. 1 but taken after electron irradiation for 15 min. Magnified images from the areas *b*, *c*, and *d* coupled with 2-D Fourier transform of the *square* regions inset showing that the lamellae fragments rolled up around a MTP with partial epitaxial relationship, as schematically indexed, in (**b**), varied interspacing of the lamellar layer due to relaxation/rolling in (**c**), and zigzag suture zone (*arrow*) of the rolled fragments in (**d**)

curved lamellar layers, which cannot be explained by the objective lens defocus of (111) and ($\overline{1}11$) reflections.) The extent of lamellae rolling around MTP/fcc also depends on the adopted laser pulses at 1.4×10^{12} W/cm^2 in vacuum. For example, corrugated lamellae were extensively developed around MTP within 100 pulses (Fig. 4a) and further developed into onions surrounding much larger-sized MTP/fcc after a total of 900 pulses (Fig. 4b). (A slight overfocus above Scherzer defocus for the MTP/fcc particle was adopted to enhance the contrast of surrounding lamellar Au, which is not a defocusing artifact as indicated by its rolling upon electron irradiation. The identity of Au roll was further supported by its much wider layer interspacing than the carbon nanotubes derived from carbon-coated collodion film upon electron dosage as addressed later.)

The lamellar Au condensates were also rolled up and self assembled, having nothing to do with MTP/fcc nanoparticles but associated with nuclei cluster (Fig. 5). BFI magnified from the separate rolls in Fig. 5a showed that they are ca. 10–20 nm in diameter and up to ca. 100 nm in length (Fig. 5b, c). SAED pattern of the assembled rolls (Fig. 5d) gives elliptic diffraction arcs/rings, which can be indexed as multiple d-spacings of the lamellar (002), according to measurement on the corresponding intensity profiles and Gauss fit (Fig. 5e). The {h0l}-type reflections and {hk0} reflections besides (002) multiples are typical to helical microtubules of graphitic carbon with *2 mm* symmetry [21]. The absence of {h0l}-type reflections and {hk0} reflections thus indicated that the individual Au layer in the roll is noncrystalline rather than a network of regular hexagons as in the case of graphitic carbon in multilayers and even monolayer with otherwise impossible 2-D lattice due to surface roughening [22]. Lattice image of the roll further revealed multiple-walled layers with a negligible hollow diameter in drastic contrast to carbon nanotubes with varied extent of hollow diameter [21]. Dislocations possibly due to a pentagon-hexagon pair analogous to that occur at the junction of two zig-zag carbon nanotubes with specified chiral index such as (17, 0) and (18, 0) [23] were commonly observed. However, it is difficult, if not possible, to determine the chirality of the present Au roll due to imperfection of the individual layers. The interspacing of the layers within the multiple-walled Au roll varies from 0.458 to 0.335 nm, corresponding to 2.18–2.98 Q^{-1} FWHH in the intensity profile (Fig. 5e). Such a wide interspacing distribution can be attributed to the presence of dislocations, which were likely generated when the lamellae with a much smaller interspacing (0.241–0.192 nm) roll into MWT with a rather small radius of curvature to induce plastic deformation under the capillarity effect. In this connection, it is of interest to note that the plasticity of ultrahigh-strength gold nanowire is characterized by strain-hardening, having dislocation motion and pile-up still operative down to diameters of

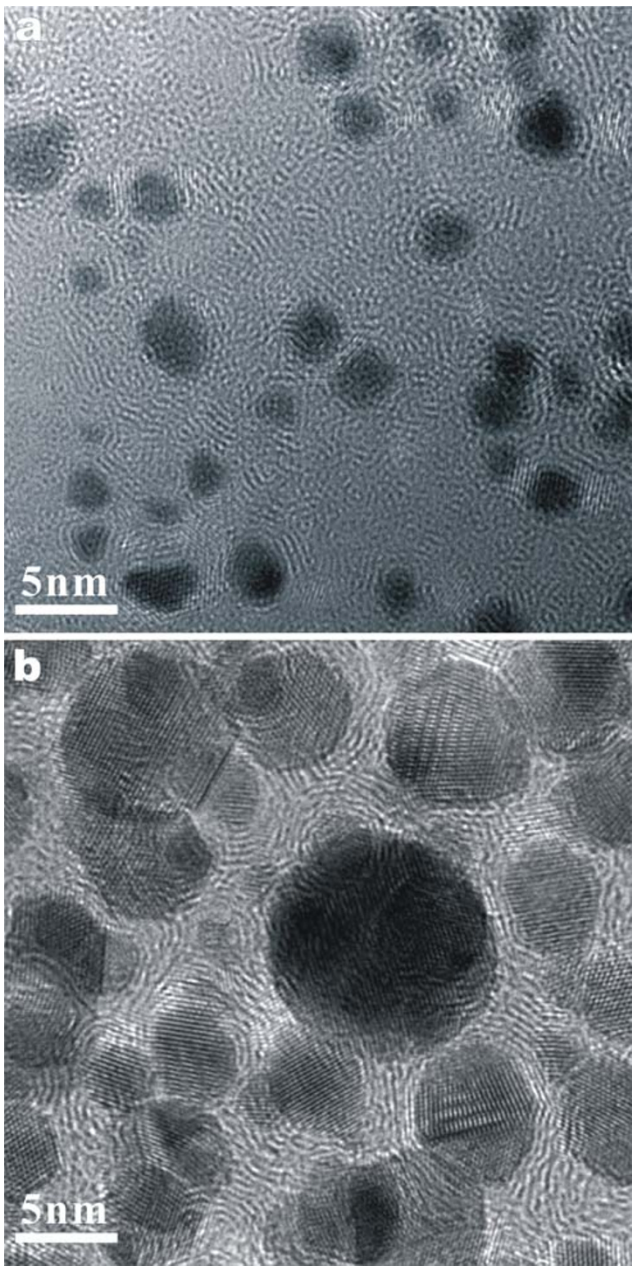

Fig. 4 Lattice images of Au **a** lamellae and **b** onions produced by laser ablation on Au target at 1.4×10^{12} W/cm^2 for 100 and 900 pulses, respectively, in vacuum. Note corrugated lamellae around MTP from place to place in (**a**), which were further developed into onions surrounding larger-sized MTP/fcc in (**b**)

40 nm [24]. Although the strength of MWT as a function of diameter is not known, pulsed radiant heating would help plastic deformation of the rolls.

Upon electron irradiation, the Au rolls are further corrugated (Fig. 6a) and separated as spherical onions (Fig. 6b) analogous to the curling and closure behavior of graphitic networks upon electron dosage [25]. It is not clear whether the defects generated in the corrugated area have anything to do with vacancy and adatom-vacancy formation as in the case involving a graphene layer [23]. It should be noted that the Au roll was unambiguously identified to have different compositions and interspacings from the graphite-like material produced by prolonged electron irradiation of the carbon-coated collodion film. The lamellae rolling around MTP/fcc, corrugated lamellae, and curved lattices observed with slight electron dosage should not be mistaken as the phase images of carbonaceous deposit on the supporting film and the surface of gold particles, or even a reconstruction of the supporting film itself under laser or electron irradiation. The carbon onion that typically formed after prolonged electron irradiation for 30 min showed a constant layer interspacing of ca. 0.33 nm (Appendix 2) rather than a much wider interspacing up to 0.45 nm for the Au tubes, which did not appear in our previous TEM observations of dense oxide condensates fabricated by the same PLA technique and collected also on carbon-coated collodion film [8]. In fact, the Au condensates fabricated by PLA in water were unambiguously found in our inter-related study to self-assemble as lamellae and then nano- to micro-diameter tubes with multiple walls when aged at room temperature in water for up to 40 days (Appendix 3).

The low-angle scattering at 1.36–1.83 Q^{-1} FWHH can be assigned as medium range order of coordination polyhedra separated at ca. 0.74–0.55 nm within the lamellar layer of the mesomorphic phase. The atoms within the layer are likely 5- and/or 6- rather than 4-coordinated in view of the structure of planar clusters of Au [26] and the fact that gold (100) film reconstructs into a (111) film below ca. 8 atomic layers, whereas the (111) film can be thinned further layer by layer [27]. (Note that the atoms within the exposed layer are 4- and 6-coordinated for gold (100) and {111}, respectively.) Since the propensity of Au_N^- clusters to favor planar structures (with N as large as 13) is correlated with strong hybridization of the atomic 5d and 6s orbitals [26], the Au lamellar nanocondensates are expected to have a semiconductor-type bonding within the layer. This argument is supported by optical absorption results of the present Au nanocondensates measured under room condition with possible H_2O signature from humid air indicating a semiconductor-type band gap. As shown in Fig. 7, the absorbance shifts from 550 to 525 nm (corresponding to 2.25–2.36 eV assuming the observed absorbance is the band-gap wavelength) for the samples with a higher content of lamella and MWT produced under progressively lower laser pulses. (A rather wide particle size range (2–10 nm) accounts for a rather broad absorption peak from 500 to 600 nm. It is not clear whether the unknown absorption around 300 nm for all the samples has anything to do with plasmon absorbance or other causes.) It should be noted that the absorption near 525 nm is well

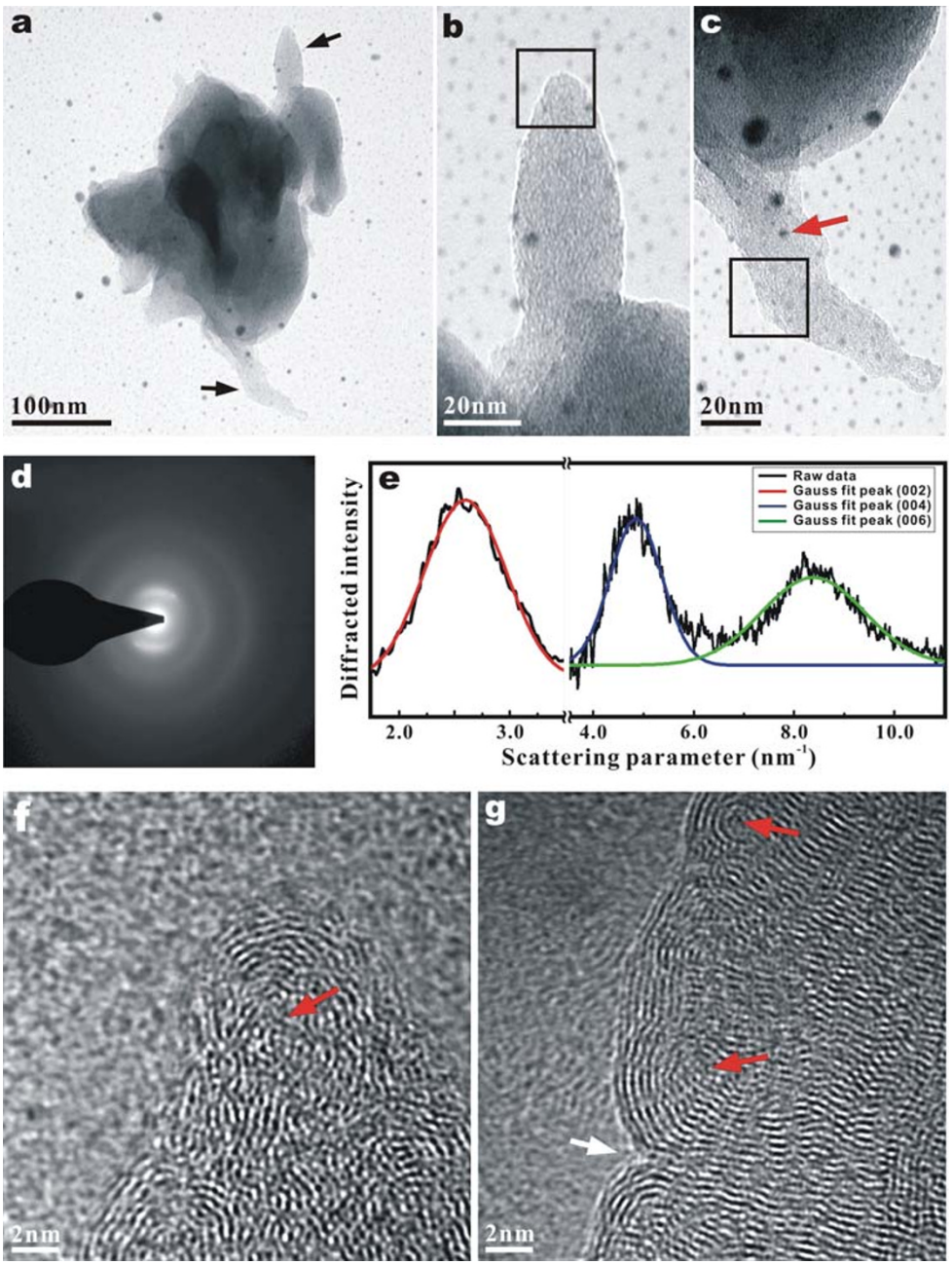

Fig. 5 TEM **a** BFI of the assembled Au lamellar rolls as produced by laser ablation, **b** and **c** magnified from separate rolls *arrowed*, **d** SAED pattern from the tangled lamellar rolls showing elliptic diffraction *arcs* and *rings* in multiple d-spacings, **e** corresponding intensity profiles and Gauss fit across the diffraction *arcs* and *rings*, **f** and **g** lattice images of separate lamellar rolls from the *square* regions in (**b**) and (**c**), respectively, with corrugated boundary *arrowed*. The nuclei cluster in the center of the tube is pointed out by an *arrow* in (**f**) and (**g**). The other objects attached to the tube wall are much larger-sized MTP/fcc particles as *arrowed* in (**c**). It is the same specimen as in Fig. 1

known for uncoated Au clusters ranging from 3 to 16 nm in size under the influence of water, according to theoretical calculation of the solvent refractive index and core charge influences on the surface plasmon absorbance [28]. Further optical absorption study of individual Au nanocondensate is required to reveal the exact absorbance contribution from the lamella, MWT, and onion. Still, the Au layers within MWT and onion are expected to have pentagon–hexagon pair near the corrugated area and dislocations to affect hybridization of the atomic orbitals and hence the optical absorption.

Discussion

Surface Stress of the Mesomorphic Lamellae

The adjacent lamellar layers of the mesomorphic phase would be attracted by Van der waals' force in order to show varied interspacing under the capillarity effect. The surface stress coefficient g acting along the plane normal direction of the lamellae can be obtained from the contraction of lattice interspacing (denoted as a) with decreasing lamellar thickness scale to particle radius (R) at

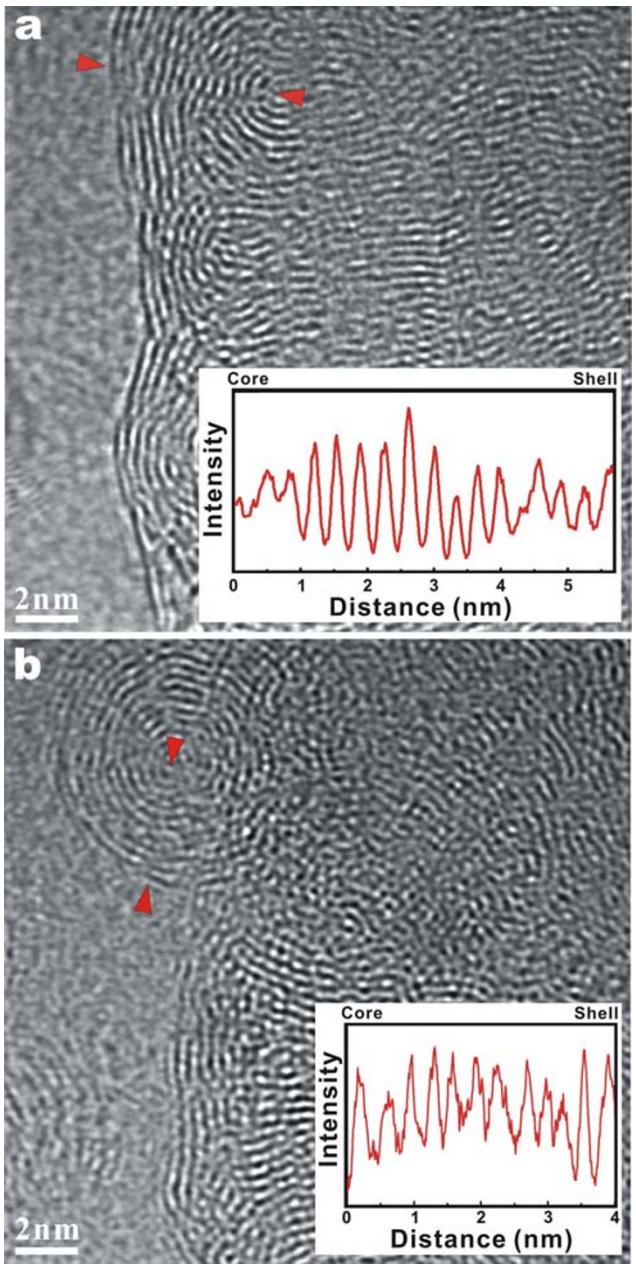

Fig. 6 **a** and **b** Lattice images of Au rolls developed from the corrugated area (*arrowed*) in Fig. 5g after electron irradiation for 1 and 5 min, respectively, showing progressive corrugation and separation into spherical onions. The intensity profiles of the lattice images along the traces *arrowed* (insets) show varied intensity and interspacings from core to shell due to dislocations and atom clusters within the onions

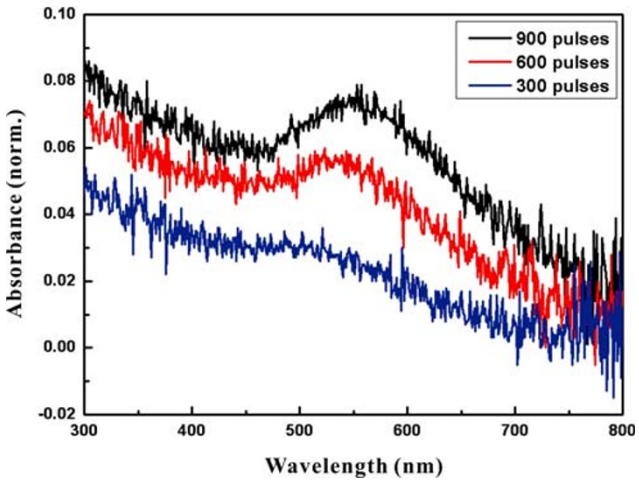

Fig. 7 Optical absorption spectrum of the Au nanocondensates produced by laser ablation on Au target at 1.4×10^{12} W/cm^2 in vacuum for 300, 600, and 900 pulses showing the surface plasmon absorbance shifts from near 525 to 550 nm for the samples produced by more pulses (cf. text)

room temperature (Fig. 2a inset). From the Laplace-type law [29], the slope of this plot is related to g by

$$\Delta a/a = -2g\kappa/3R$$

where k is the isothermal compressibility. This plot yields a reasonable value of $g \sim 0.61$ N m^{-1} for the lateral surface of the lamellae if κ is nearly two orders of magnitude higher than that of bulk fcc and hcp under the capillarity effect besides Van der waals' attraction. (In general, Van der waals' attraction is nearly two orders of magnitude weaker than metallic bonding [30].) The latter are valued at $\kappa = 5.18 \times 10^{-12}$ and 5.24×10^{-12} m^2 N^{-1}, i.e., an incompressibility of 193 and 191 GPa, respectively, according to local density approximation calculation [31]. Such a surface stress coefficient (0.61 N m^{-1}) for the lateral surface of the lamellae is then reasonably lower than the experimental and theoretical values of more rigid fcc, either nano or bulk as compiled in Table 1 of Ref. [29]. (According to this table, $g_{(220)} = 3.08 \pm 0.7$ N m^{-1} and $g_{(422)} = 3.19 \pm 1$ N m^{-1} for fcc nanocrystals, and the surface tension coefficient $\gamma_{(111)}$ =1.97 J m^{-2} from broken bonds model.) The surface stress of the mesomorphic lamella would be further complicated by the elastic anisotropy of MTP, in particular its disclination and shear gradient as observed in decahedral Au nanoparticles [32], when the two phases were adjoined in partial epitaxial relationship. However, it is by no means clear if monolayer Au can sustain such unusual elastic properties and strength as in the case of monolayer grapheme [33].

Formation Mechanisms of Au Lamellae/Rolls

Thermodynamically, the formation of Au lamellar nanocondensates in the present laser ablation process involves nucleation, growth, and impingement stages as depicted schematically in Fig. 8. This scenario, though yet to be proved by in situ observations, is in accordance with the observed microstructures in Figs. 2, 3, 4 and laser pulse dependence of phase and size of the Au nanocondensates

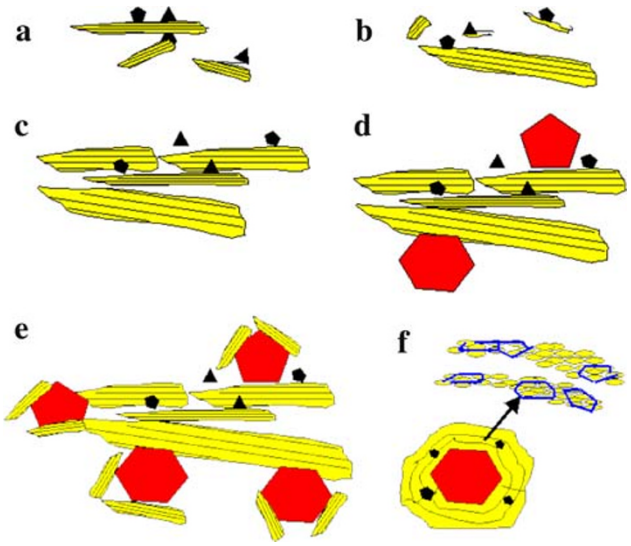

Fig. 8 Schematic drawing of the development of Au lamellar nanocondensates: **a** bulk nucleation from Au clusters denoted as *dark polyhedra*, **b** coarsening via capillarity effect, **c** Brownian motion/rotation of imperfectly attached domains, **d** epitaxial nucleation of Ih/Dh (denoted as large *red polyhedra*) from lamellar domains, **e** explosive nucleation of lamellar fragments due to heterogeneous catalysis by well developed {111} of Ih/Dh. **f** Lamellae with 5- and 6-coordinated atoms within the layer and van der waals' attraction between the layers roll up upon electron irradiation

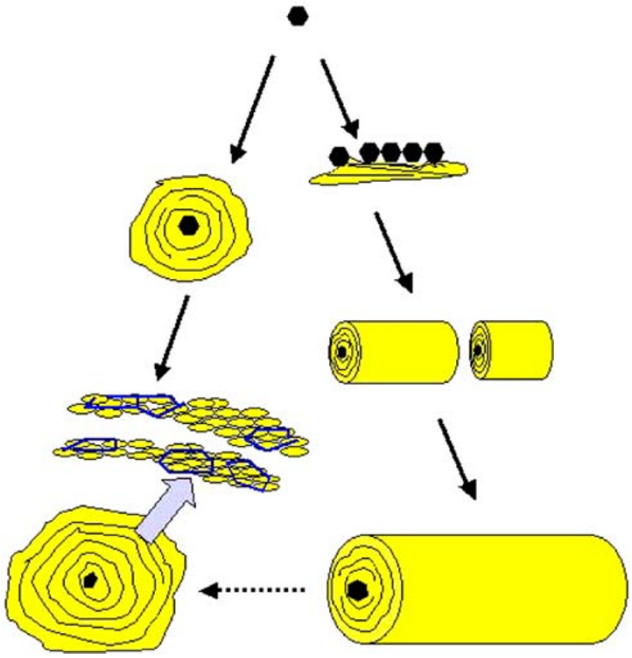

Fig. 9 Schematic drawing of the development of Au onion and MWT. The lamellae in partial epitaxy with a single-atom cluster and/or cage would *roll up* and coarsen to form an onion (*left*); whereas the lamellae in partial epitaxy with a number of atom clusters and/or cages would develop into uncapped MWT via anisotropic growth and/or a coalescence process. The uncapped MWT tended to change into onion (*dotted arrow*) for dangling bonds reduction upon electron irradiation. The onion shell with 5- and 6-coordinated atoms within the layer and van der waals' attraction between the layers are magnified as the case in Fig. 8f

as compiled in Table 1. The supercooled liquid with Au clusters in planar, cage, or pyramid forms [7, 34] would facilitate bulk nucleation of the lamellae (Fig. 8a). In fact, the change of 3-D clusters into planar structure involves strong hybridization of the atomic 5d and 6s orbitals as mentioned [26]. Pressure and residual stress as a result of extremely rapid heating and cooling under a very high-power density input would cause a higher coordination of the melt, analogous to the case of alkali-germanate melts under static high-temperature high-pressure (HTHP) conditions [35], and hence the nucleation of the lamellae as would otherwise not be observed. Such a dynamic HTHP route apparently did not reach the stability field of a hexagonal-close-packed (hcp) structure experimentally determined to be above $\sim$240 GPa [36]. The lamellar phase cannot be derived from hcp-Au because it always back-transforms into fcc structure upon rapid quenching [36]. Subsequent coarsening and lateral growth of the lamella (Fig. 8b) would proceed under the combined effects of capillarity force and structural ledge movement. The impinged lamellar nanocondensates could change their orientations via a Brownian motion/rotation process, in order to form a larger unity (Fig. 8c) analogous to {hkl}-specific coalescence of TiO_2 rutile nanocondensates [37]. The well-developed lamella would then facilitate partial epitaxial nucleation of MTP (Fig. 8d). It should be noted that the lamellae can originate from 3D atom clusters in a bulk nucleation event (Fig. 8a) or alternatively by partial epitaxial nucleation on much larger-sized MTPs in a heterogeneous nucleation event (Fig. 8e) for further formation of onion-like shells (Fig. 8f). In this connection, the Au MTPs were found to transform into fcc by the catalytic effect of a partial epitaxial graphite-like material formed during in situ TEM observations [9]. Such a partial epitaxy nucleation event was also observed in the diamond films on Si{111} planes [38]. By contrast, the direct condensation of MWT or onions of Au has nothing to do with MTPs. Their formation was likely facilitated by some atom clusters at their center analogous to the effect of C_{60} on graphene derived materials [25]. This scenario, based on the observations in Figs. 5 and 6, is depicted in Fig. 9, which shows a partial epitaxial nucleation event of lamellae on a single atom cluster/cage with a diameter around 0.4–0.5 nm (Figs. 5f, g, 6) followed by rolling and coarsening to minimize the surface area as for an onion. On the other hand, the lamellae in partial epitaxy with many such nuclei would roll up and extend by anisotropic growth and coalescence to form uncapped MWT. Further electron

irradiation would turn it into onions for dangling bonds reduction.

Kinetically, the formation and retention of the lamellar nanocondensates with a density higher than individual atom clusters depend on rapid heating and cooling for a pressure effect as the case of the formation of dense α-PbO_2-type TiO_2 nanocondensates [8]. The cooling rate u of the individual Au condensate depends on its size, temperature, and heat capacity as well as radiant emissivity of specific phase. Assuming that gray body radiation [39] for a PLA process [40] and the physical properties of fcc bulk [39, 41] are valid for the stable fcc condensates, u was estimated to be in the range of 10^6–10^7 K/s depending on particle size. The cooling rate for nonstable/metastable Au nanocondensates is likely much higher because size miniature would enhance heat conduction in nanofluids [42] and Au clusters are frozen to Ih structure at a cooling rate as high as 10^{11} K/s, according to molecular dynamic simulation [43]. In any case, the molten Au would be supercooled as nonstable clusters/lamellae and metastable Ih/Dh at specific glass transition temperatures (T_g), whereas stable fcc structure with drastic volume and enthalpy changes at melting point (T_m) in the present dynamic cooling process. A smaller condensate size may lower T_m and T_g under the influence of capillarity effect, i.e., surface tension and surface stress, respectively, as mentioned.

Conclusions

As a final remark, the theoretically predicted planar liquid phase [7] can be as large as the present mesomorphic Au lamellae under the condition of experimentally realizable cooling rates. Au lamellar nanocondensates would be a promising precursor of tubular or onion-like materials via an electron/photon excitation route or in the presence of stabilizers/ligands for potential biomedical, optoelectronic, and catalytic applications. The synthesis of such tubular Au is encouraged by this study and previous report on helical gold rolling into multi-shell nanowire [44] and nanotube [45] via a top-down approach, i.e., electron-beam thinning.

Acknowledgments We thank Dr. A. C. Su for helpful discussion on mesomorphic phase, Dr. R. H. Hsu for the help on optical absorbance spectrum, Mr. Jacob Chu for reading the manuscript, and anonymous referees for constructive comments. This work was supported by Center for Nanoscience and Nanotechnology at NSYSU and partly by National Science Council, Taiwan, ROC under contract NSC98-2221-E-110-040-MY3.

Appendix 1

See Fig. 10.

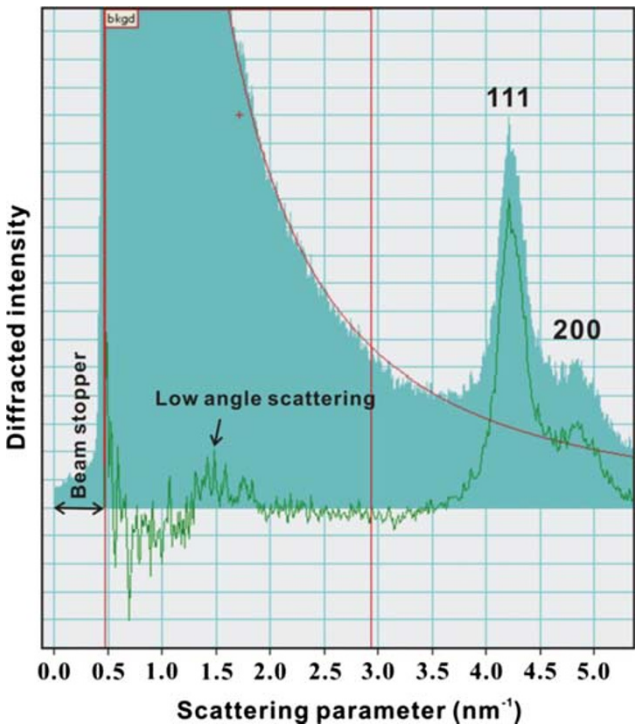

Fig. 10 Diffracted intensity profile (*cyan shadow*) taken from the inset of Fig. 1a showing a maximum intensity around the axis (0 nm^{-1}) before background subtraction to reveal a low-angle scattering bump in the profile (*green*) as the case in Fig. 1d

Appendix 2

See Fig. 11.

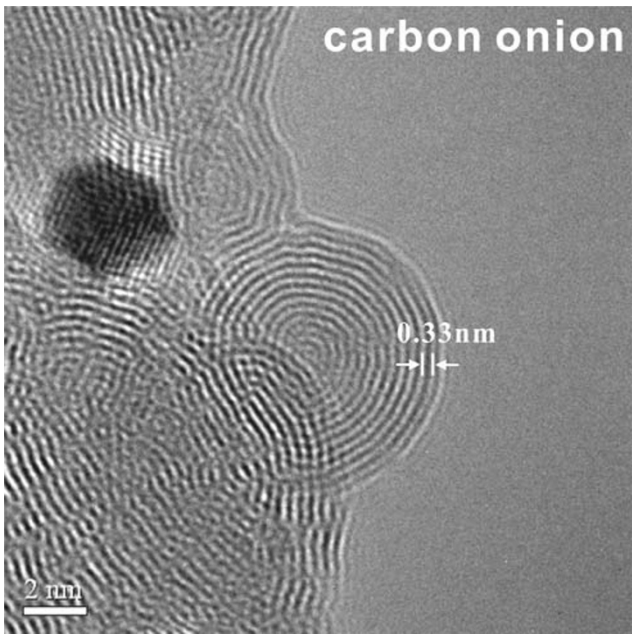

Fig. 11 HREM image of the carbon onion with a constant layer interspacing (ca. 0.33 nm), which was typically formed after prolonged (>30 min) electron irradiation on a carbon-coated collodion film in this study

Appendix 3

See Fig. 12.

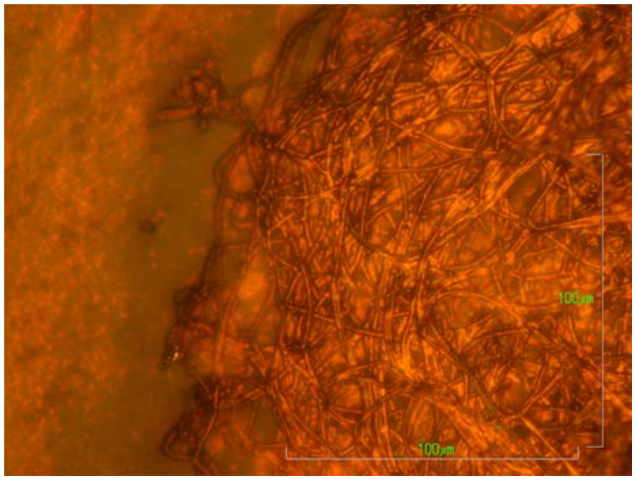

Fig. 12 Optical micrograph of Au tubes with micro-diameter and multiple walls that were very extended in length and hence entangled with each other. Such tubular materials were developed from the lamellar condensates fabricated by PLA in water followed by aqueous aging at room temperature for up to 40 days in our inter-related study [10]

References

1. S. Iijima, T. Ichihashi, Phys. Rev. Lett. **56**, 616 (1986)
2. P.A. Buffat, M. Flüeli, R. Spycher, P. Stadelmann, J.P. Borel, Faraday Discuss. **92**, 173 (1991)
3. M.P. Johansson, D. Sundholm, J. Vaara, Angew. Chem. Int. Ed. Engl. **43**, 2678 (2004)
4. X. Gu, M. Ji, S.H. Wei, X.G. Gong, Phys. Rev. B **70**, 205401 (2004)
5. S. Bulusu, X. Li, L.S. Wang, X.C. Zeng, PNAS **103**, 8326 (2006)
6. R. W. Siegel, Phys. Today **46**, 64 (1993)
7. P. Koskinen, H. Häkkinen, B. Huber, B.V. Issendorff, M. Moseler, Phys. Rev. Lett. **98**, 015701 (2007)
8. S.Y. Chen, P. Shen, Phys. Rev. Lett. **89**, 096106 (2002)
9. C.N. Huang, S.Y. Chen, Y. Zheng, P. Shen, J. Phys. Chem. C **112**, 14965 (2008)
10. C.N. Huang, S.Y. Chen, Y. Zheng, P. Shen, Nanoscale Res. Lett. (2009). doi:10.1007/s11671-009-9359-x
11. A. Masson, J.J. Métois, R. Kern, Surf. Sci. **27**, 463 (1971)
12. J.J. Métois, M. Gauch, A. Masson, R. Kern, Thin Solid Films **11**, 205 (1972)
13. J. Rankin, J. Am. Ceram. Soc. **82**, 1560 (1999)
14. H. Yasuda, H. Mori, J. Electron Microsc. **48**, 581 (1999)
15. H. Yasuda, K. Furuya, Philos. Mag. A **80**, 2355 (2000)
16. K. Nonaka, K. Kohra, J. Phys. Soc. Jpn. **9**, 512 (1954)
17. T. Suzuki, J. Phys. Soc. Jpn. **10**, 1026 (1955)
18. B.D. Hall, J. Appl. Phys. **87**, 1666 (2000)
19. C.Y. Ruan, Y. Murooka, R.K. Raman, R.A. Murdick, Nano Lett. **7**, 1290 (2007)
20. D.B. Williams, C.B. Carter, *Transmission Electron Microscopy—Spectrometry IV* (Plenum Press, New York, 1996)
21. S. Iijima, Nature **354**, 56 (1991)
22. J.C. Meyer, A.K. Geim, M.I. Katsnelson, K.S. Novoselov, T.J. Booth, S. Roth, Nature **446**, 60 (2007)
23. A. Hashimoto, K. Suenaga, A. Gloter, K. Urita, S. Iijima, Nature **430**, 870 (2004)
24. B. Wu, A. Heidelberg, J.J. Boland, Nat. Mater. **4**, 525 (2005)
25. D. Ugarte, Nature **359**, 707 (1992)
26. H. Häkkinen, M. Moseler, U. Landman, Phys. Rev. Lett. **89**, 033401 (2002)
27. Y. Kondo, Q. Ru, K. Takayanagi, Phys. Rev. Lett. **82**, 751 (1999)
28. A.C. Templeton, J.J. Pietron, R.W. Murray, P. Mulvaney, J. Phys. Chem. B **104**, 564 (2000)
29. C. Solliard, M. Flueli, Surf. Sci. **156**, 487 (1985)
30. S.M. Allen, E.L. Thomas, *The Structure of Materials* (Wiley, New York, 1999)
31. R. Ahuja, S. Rekhi, B. Johansson, Phys. Rev. B **63**, 212101 (2001)
32. C.L. Johnson, E. Snoeck, M. Ezcurdia, B. Rodriguez-Gonzales, I. Pastoriza-Santos, L.M. Liz-Marzan, M.J. Hÿtch, Nat. Mater. **7**, 120 (2008)
33. C. Lee, X. Wei, J.W. Kysar, J. Hone, Science **321**, 385 (2008)
34. H. Häkkinen, M. Moseler, O. Kostko, N. Morgner, M.A. Hoffmann, B.V. Issendorff, Phys. Rev. Lett. **93**, 093401 (2004)
35. D.L. Farber, Q. Williams, Science **256**, 1427 (1992)
36. L. Dubrovinsky, N. Dubrovinskaia, W.A. Crichton, A.S. Mikhaylushkin, S.I. Simak, I.A. Abrikosov, J.S. de Almeida, R. Ahuja, W. Luo, B. Johansson, Phys. Rev. Lett. **98**, 045503 (2007)
37. M.H. Tsai, S.Y. Chen, P. Shen, Nano Lett. **4**, 1197 (2004)
38. S.T. Lee, H.Y. Peng, X.T. Zhous, N. Wang, C.S. Lee, I. Bello, Y. Lifshitz, Science **287**, 104 (2000)
39. G. Chryssolouris, *Laser Machining—Theory and Practice* (Springer, New York, 1991)
40. D.B. Chrisey, G.K. Hubler, *Pulsed Laser Deposition of Thin Films* (Wiley, New York, 1994)
41. I. Barin, *Thermochemical Data of Pure Substances Part I Ag-Kr*. (VCH Verlagsgasellschsft mbH D-6940 Weinheim, Federal Republic of Germany, 1993)
42. D.H. Kumar, H.E. Patel, V.R.R. Kumar, T. Sundararajan, T. Pradeep, S.K. Das, Phys. Rev. Lett. **93**, 144301 (2004)
43. H.S. Nam, N.M. Hwang, B.D. Yu, J.K. Yoon, Phys. Rev. Lett. **89**, 275502 (2002)
44. Y. Kondo, K. Takayanagi, Science **289**, 606 (2000)
45. Y. Oshima, A. Onga, K. Takayanagi, Phys. Rev. Lett. **91**, 205503 (2003)